Energy Conversion and Management 311 (2024) 118519

Contents lists available at ScienceDirect

Energy Conversion and Management

journal homepage: www.elsevier.com/locate/enconman

Research Paper

CHESTER: Experimental prototype of a compressed heat energy storage and management system for energy from renewable sources

K. Theologou [a,*], M. Johnson [a], J. Tombrink [a], José L. Corrales Ciganda [b], Felipe T. Trebilcock [b], K. Couvreur [c], R. Tassenoy [c], S. Lecompte [c,d]

[a] DLR, Institute of Engineering Thermodynamics, Pfaffenwaldring 38-40, 70569 Stuttgart, Germany
[b] Tecnalia Research & Innovation, Area Anardi 5, Azpeitia, Guipuzkoa 20730, Spain
[c] Ghent University, Sint-Pietersnieuwstraat 41, 9000 Ghent, Belgium
[d] FlandersMake@UGent – Core Lab EEDT-MP, flandersmake.be, Belgium

ARTICLE INFO

Keywords:
Thermo-mechanical energy storage (TMES)
Carnot battery (CB)
Thermally integrated pumped thermal energy storage (TI-PTES)
Compressed heat energy storage (CHEST)
Experimental laboratory CHESTER prototype
Electricity- and heat sector coupling

ABSTRACT

The increasing share of renewable energies in the electricity grid requires storage technologies to balance energy supply and demand. Thermally integrated pumped thermal energy storage systems are considered a promising technology for medium to large-scale storage applications. Among these, compressed thermal energy storage in particular has been identified in numerous theoretical studies as a promising candidate. Despite these studies, the feasibility of the thus far theoretical concept has not yet been proven experimentally. To overcome this gap this publication presents for the first time the entire setup and experimental results of the world's first CHESTER (Compressed Heat Energy Storage for Energy from Renewable Sources) laboratory prototype at a representative scale consisting of a high-temperature heat pump and an organic Rankine cycle coupled by a combination of a sensible and a novel dual-tube latent heat storage as a high-temperature thermal energy storage system. The stable operation of a fully integrated CHEST system on a 10 kW scale was demonstrated and the stable function of the latent heat storage unit as both a condenser and an evaporator was confirmed. With the current prototype, which combines three first of its kind subsystems, efficiencies of up to 37 % have been achieved. The presented results confirm the practical feasibility of the thus far theoretical concept and provide guidance for further optimization of the components and more importantly the interaction between the individual subsystems.

Nomenclature

Variables	
COP	coefficient of performance [-]
E	Energy [kWh]
h	specific enthalpy [kJ/kg]
L	fill level [m]
$\dot{m}$	mass flow rate [kg/s]
n	rotational speed [1/m]
P	electrical power [W]
p	pressure [bar]
$\dot{Q}$	heat flow rate [W]
s	specific entropy [kJ/(kgK)]
T	temperature [°C] or [K]
$\dot{V}$	volume flow rate [m^3/s]
Greek	
ε_{net}	net power ratio [-]
η_{RT}	roundtrip efficiency [-]

(*continued on next column*)

(*continued*)

η_{net}	roundtrip utilization rate [-]
ϱ	density [kg/m^3]
Abbreviations	
CB	Carnot battery
CHEST (ER)	compressed heat energy storage (for Energy from Renewable Sources)
DLR	German Aerospace Center
HT-HP	high-temperature heat pump
HT-TESS	high-temperature thermal energy storage system
LH-TES	latent heat thermal energy storage
ORC	organic Rankine cycle
PCM	phase change materials
SH-TES	sensible heat thermal energy storage
(TI-)PTES	(thermally integrated) pumped thermal energy storage
TMES	thermo-mechanical energy storage
Subscripts	
C	heat input process/cycle

(*continued on next page*)

* Corresponding author.
E-mail address: konstantinos.theologou@dlr.de (K. Theologou).

https://doi.org/10.1016/j.enconman.2024.118519
Received 29 November 2023; Received in revised form 25 March 2024; Accepted 3 May 2024
Available online 17 May 2024

(*continued*)

LH	LH-TES
SH	SH-TES
so	heat source
co	compressor
D	dispatching process/cycle
si	heat sink
off	offset
in	inlet
out	outlet
ex	expander
pu	pump
i	time period
j	seconds
ht	hot water tank
ct	cold water tank
wat	water
ref	refrigerant
TESS	thermal energy storage system

1. Introduction

Following the Paris Agreement, the European Union aims to achieve an economy with net zero greenhouse gas emissions by 2050 with the European Green Deal [1]. In this context, a strategy is being pursued to reduce greenhouse gas emissions, improve energy efficiency and increase the share of renewable energy by 2030 [2]. Integrating fluctuating renewable energy sources, e.g. photovoltaics and wind power, into the electricity grid of the energy system is one major challenge [3]. In addition, efforts to substitute fossil fuels with renewable energy sources for the heating and cooling sector must also be increased, e.g. with heat pumps, to achieve the climate targets [4]. For integrating a very high share of renewable energy sources into the electricity grid, heating and cooling sectors, energy storage systems are essential [5]. In particular, cross-sector solutions coupling the electricity and heat sectors with smart energy storage systems are seen to offer great potential for increasing the flexibility of the electricity grid [6]. For this purpose, the development and investigation of thermo-mechanical energy storage (TMES) have become an important research focus in terms of grid scale and long-duration energy storage systems [7]. A categorisation of the different types of TMES is provided by Olympios et al. [8]. In recent years, the term *Carnot Battery* (CB), a concept that includes a cluster of TMES has been introduced [9]. The publications that most thoroughly define the term and the technologies under the Carnot Battery umbrella were published by Dumont et al. [10].

One of the most promising CB solutions in terms of system efficiency and flexibility has turned out to be the pumped thermal energy storage (PTES) [11]. It is also referred to pumped thermal electricity storage [12]. The PTES is characterised by the use of a heat pump for creating a temperature lift for energy conversion and storage. When dispatching the energy, a heat engine converts thermal to electrical energy. This can theoretically be realised either by an additional thermodynamic cycle or by a reversible heat pump / organic Rankine cycle system [13]. A combination of a heat pump with thermal energy storage can achieve an ideal round-trip efficiency of up to 100 % [14]. Zhao et al. [15] show that the roundtrip efficiency of their PTES model is higher in a combined heat and electricity mode as an energy management system supplying electricity and multi-grade thermal energy than in a pure electricity storage mode. If the heat pump uses waste heat, district heat, solar thermal heat or other heat supply systems at low and medium temperature levels for operation, it is referred to as thermally integrated PTES (TI-PTES) [16]. Theoretical studies show that especially TI-PTES have great potential. Dumont and Lemort [17] compare TI-PTES with other energy storage technologies and conclude that TI-PTES theoretically have a high potential because of their high roundtrip efficiency, low specific price and long lifetime. While PTES have no geographical restrictions, TI-PTES have a low geographical dependency due to thermal integration, which is usually associated with a good connection to the electricity grid or district heating networks. In contrast, pumped hydro energy storage is strongly dependent on the topography and compressed air energy storage on the underground geological conditions. Frate et al. [18] show in a thermo-economic study that TI-PTES may be economical as large-scale and long-duration energy storage. In another thermo-economic study, Hu et al. [16] found that in terms of minimum storage costs, TI-PTES are better suited for coupling with waste heat than for coupling with district heating networks or solar thermal scenarios. A recent literature overview of TI-PTES system configurations is given by Zhang et al. [19], who created a configuration selection map. Benato and Stoppato [20] distinguish the PTES technologies between closed Brayton or reversible Brayton cycles, the transcritical organic Rankine cycle with CO_2 as the working fluid, and the compressed heat energy storage (CHEST). In a review of TI-PTES, Frate et al. [21] summarise that while there is a lot of theoretical work done with conceptual studies and simulations, there is a lack of experimental data for validation because there are no existing TI-PTES prototypes. Steinmann [22] points out that there is a lack of PTES prototypes because essential components such as efficient high temperature compressors or efficient CO_2 engines are not commercially available. Based on this finding, Steinmann [22] introduces the first CHEST approach as a PTES with conventional subcritical Rankine cycles and state-of-the-art components.

The CHEST concept, which can be designed as a PTES or TI-PTES, is, according to Steinmann [22], characterised by latent heat thermal energy storage using phase change materials (PCM) to increase efficiency by minimizing the temperature differences during the evaporation and condensation process between the working fluid and the storage medium. The thermal energy storage can be combined with a sensible unit to achieve effective use of the sensible heat after the condensation process by subcooling and before the evaporation process by preheating the working fluid. Tafone et al. [23] investigated numerically the CHEST system with a cascade of multiple PCMs and calculated a round trip efficiency of 47.6 % for their model. In the first CHEST approach, Steinmann [22] suggests a cascaded compression with six stages (ammonia and water as the working fluids) and a combination of sensible and latent heat thermal energy storages at temperatures between 200 and 400 °C. Later, Jockenhöfer et al. [24] further developed the CHEST concept with a low temperature thermal integration, able to convert electrical and thermal energy and with an optional connection to a smart district heating network. The authors use butene as the working fluid for the heat pump and the heat engine and a combination of sensible and latent heat thermal energy storage with a eutectic mixture of potassium nitrate and lithium nitrate having a melting point at 133 °C. The numerical results show a net energy ratio of 125 % at a heat source temperature of 100 °C and a heat sink temperature of 15 °C. The maximum exergetic efficiency of 59 % is achieved when thermal and electrical energy is supplied. For the same CHEST concept, Hassan et al. [25] found, after several parametric studies, that R1233zd(E) and R1234ze(D) are the most promising working fluids when the same fluid is used for the heat pump and the heat engine sides. For the use of two different working fluids, it was determined that R1233zd(E) achieves the best system performance for the heat pump side and butene for the heat engine side. Frate et al. [26] also found in their simulations that R1233zd(E) is the most promising fluid for their TI-PTES concept. These theoretical studies show the possibilities of the TI-PTES system. Systems that use separate working fluids for the two conversion cycles have, on the one hand, the advantage that each of the thermodynamic cycles can be optimised. On the other hand, the use of one working fluid can lead to fewer components. Lund [27] addresses the advantages of the CHEST concept as part of a smart energy system in combination with a district heating system, allowing the utilisation of synergy effects between the operation of the heat and electrical side of the storage system. The author investigates the benefits of the CHEST concept in a theoretical energy system scenario for Germany for the year 2050, where the power production is characterised by a large share of renewable energy in the form of wind power and photovoltaic and compares the concept with a

Li–ion battery. The CHEST concept was analysed in different model configurations, without district heating and using district heating in an electric heating scenario via heat pumps or in a fuel heating scenario via fuel boilers. Regarding the reduction of the primary energy supply, the preferred application use case is the electrical district heating scenario. Another energy system scenario with the CHEST concept based on a high temperature heat pump is presented in Sánchez-Canales et al. [28] for potential integration with a 26 MW wind farm in the Spanish electricity market, also considering the technical constraints. By varying the thermal energy storage capacities and the size of the CHEST model, according to the simulation, the system provides up to 20 % of the power plants total energy contribution. A recent publication by Novotny et al. [29] maps the PTES technologies under commercial development and places them in the perspective of related scientific works. In 2020, Frate et al. [21] stated that there are no existing TI-PTES prototypes tested in the laboratory or demonstrated with pilot systems. For this reason, and to push the technological level of TI–PTES, the innovative system concept CHESTER (CHEST for Energy from Renewable Sources) was developed to create a very flexible and smart renewable energy management system.

Based on the identified lack of PTES prototypes, the present work presents for the first time an entire setup and experimental results of the first laboratory prototype of a CHEST system. The aim is to assess the feasibility of integrating three first of its kind subsystems into a single system as well as the stability of the entire system. The experimental results obtained provide insights and an understanding of the interaction of the individual subsystems. Although the laboratory prototype cannot make any statement about the maximum efficiency of the concept due to the downscaling and the maximum temperatures limited to the current development level of the heat pump, this work is nevertheless an important milestone that will help drive further technical development of the CHEST concept.

2. Description of the laboratory prototype

CHESTER is an energy storage and management system based on the TI-PTES technology, which converts electrical energy and low-temperature heat to high-temperature heat via a heat pump. The high-temperature heat is stored and, when necessary, converted back to electrical energy by a power cycle. In addition to providing dispatchable electrical energy, both electrical and thermal energy for heating or process heat can be provided. The conversion of electrical to thermal energy with the use of a heat pump also offers flexibility for thermal integration. Different scenarios and application use cases for the implementation of the CHEST concept, each with characteristic values, are given in detail by Steinmann et al. [30]. As an example, a general scenario of the CHESTER energy storage and management system with a smart district heating system is shown in Fig. 1. Smart district heating systems use solar thermal energy or other energy sources to supply domestic heat. The time discrepancy between availability and demand can be compensated by short-term water storages or by seasonal thermal energy storages, as currently operating in several systems in Denmark. In the example scenario, CHESTER uses excess electricity from wind and solar energy to drive a heat pump (Fig. 1, left), converting this electricity to heat and storing this heat in the storage system. Seasonal thermal energy storage can be used as a heat source for the heat pump. During dispatching (Fig. 1, right), an organic Rankine cycle generates electricity for the power grid from the thermal energy transferred out of the storage system and transports excess heat back into the seasonal thermal energy storage [30].

2.1. System integration in the laboratory

Fig. 2 shows a simplified flow diagram of the CHESTER laboratory prototype, installed in the DLR (German Aerospace Center) laboratories. The prototype is designed for an electrical power output of

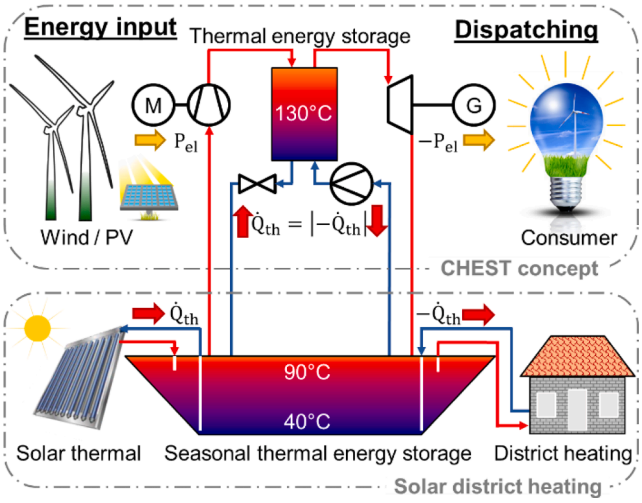

Fig. 1. CHESTER with smart district heating system, showing the system charging with heat upgrade on the left and system discharging with energy dispatch on the right.

approximately 10 kW_{el} and combines for the first time three innovative subsystems: a high-temperature heat pump (HT-HP) operating up to 150 °C, a high-temperature thermal energy storage system (HT-TESS) with a novel directly integrated dual-tube latent heat storage as a condenser and evaporator and an organic Rankine cycle (ORC) with a variable volume ratio expander.

For the heat upgrade and energy input cycle on the left, the HT-HP upgrades the heat of the low-temperature heat source to a temperature above the melting temperature of the PCM used in the LH-TES, thereby charging the storage system. For the prototype, the electrical network of the laboratory is used. The heat source is a hot water tank with an electric heater with a power of 100 kW_{el} and a temperature range of 40 to 100 °C. In the middle, the HT-TESS is shown, consisting of latent heat thermal energy storage (LH-TES) and sensible heat thermal energy storage (SH-TES). In the LH-TES, the working fluid is condensed during the HT-HP operation, which transfers heat and charges the storage system. During the energy dispatching operation of the ORC and thereby discharging the HT-TESS, the LH-TES serves as an evaporator. The sensible heat for subcooling in the HT-HP cycle and preheating in the ORC cycle is stored in and provided by the SH-TES. For the energy dispatching cycle on the right, the ORC transforms heat into electricity. The electricity generated by the prototype is fed directly into the electrical grid. The cooling water network of the laboratory is used as the heat sink for the ORC condenser, which enables temperature regulation; in the experiments, the inlet temperature was regulated to 25 °C. Furthermore, there is no communication between the heat sink and the heat source in the laboratory. Fig. 3 shows a picture of the CHESTER

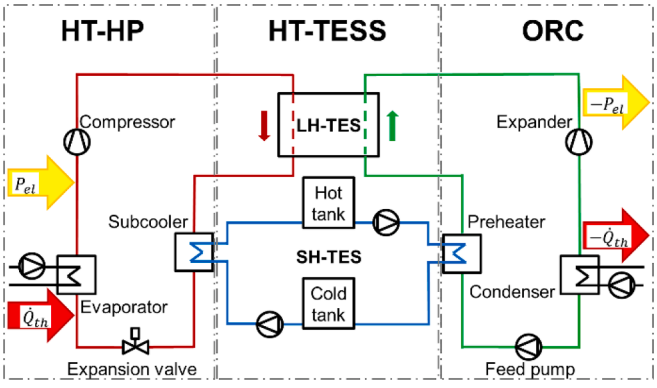

Fig. 2. Simplified flow diagram of the CHESTER laboratory prototype.

prototype in the laboratory from the perspective of the HT-HP. The ORC is behind the LH-TES and depicted in an inserted frame.

2.2. Selection of phase change material, refrigerants and lubricants

The PCM used in the LH-TES was selected to have a melting temperature below 160 °C, due to the limitation in available HT-HPs operating above that limit [31]. A eutectic mixture of $LiNO_3$ and KNO_3 with a theoretical phase change temperature of 133 °C was selected. The PCM mixture ratio was 33 wt% $LiNO_3$ and 67 wt% KNO_3, following Guizane et al. [32] and Tamme et al. [33]. During commissioning, it was observed that the PCM melts in a temperature range from approximately 128 to 136 °C, showing that the eutectic mixture was not attained. This may be due to incorrect mixing or inaccurate literature data. Roget et al. [34] show in their publication that the composition of the eutectic mixture of $LiNO_3$ and KNO_3 in the literature is inconsistent and dispersed.

As can be seen schematically in Fig. 2, a dual-tube design of the LH–TES should be used when the thermodynamic cycles use two different refrigerants as working fluids. This way, the refrigerant can be optimally matched to the thermodynamic cycles of the HT-HP and ORC subsystems respectively, and lubricant migration or mixing can be avoided [35]. The selection of the refrigerant determines the shape of the two-phase area in the T-s diagram of the nominal charging and discharging cycles, as shown in Fig. 4. R1233zd(E), with a critical pressure of 36.2 bar and a critical temperature of 166.5 °C, is selected for the HT-HP; R1336mzz(E), with a critical pressure and temperature of 31.5 bar and 137.7 °C, respectively, is selected for the ORC [36].

R1233zd(E) was selected for the heat upgrade and energy input cycle with the HT-HP to obtain the best possible thermodynamic performance for the nominal boundary conditions [25]. To avoid large superheating for the ORC, which requires additional heat transfer area and has an impact on performance, a so-called dry fluid (R1336mzz(E)) was used with the slope of the saturation curve sloped inwards. R1233zd(E) on the other hand is an isotropic fluid with a semi-vertical slope of the saturated vapour curve on the T-s diagram (Fig. 4, top). It has a global warming potential of 1 and an ozone depletion potential of nearly 0 [31]. It belongs to the Hydro-Chloro-Fluoro-Olefins group and is non-flammable. The HT-HP compressor lubricant is the Reniso Triton SEZ320. It is a synthetic polyolester oil specifically designed to be used with fluorinated hydrocarbons. Experimental pre-tests to investigate the interaction between R1233zd(E) and Reniso Triton SEZ320 show that the refrigerant-lubricant mixture meets the criteria for viscosity well.

For the energy dispatching cycle with the ORC, R1336mzz(E) was selected as the refrigerant. It belongs to the Hydro-Fluoro-Olefins group. This refrigerant has favourable chemical properties such as low toxicity, low flammability, and a global warming potential of 18 with an ozone depletion potential of 0 [31]. Within the refrigerants with suitable chemical properties, R1336mzz(E) was selected based on thermodynamic cycle simulations to maximize the expander power output and cycle efficiency in the expected operating range. The ORC expander lubricant is Reniso Triton SEZ220. This lubricant was selected based on its miscibility with the refrigerant, having a viscosity suitable for expander operation at higher temperatures.

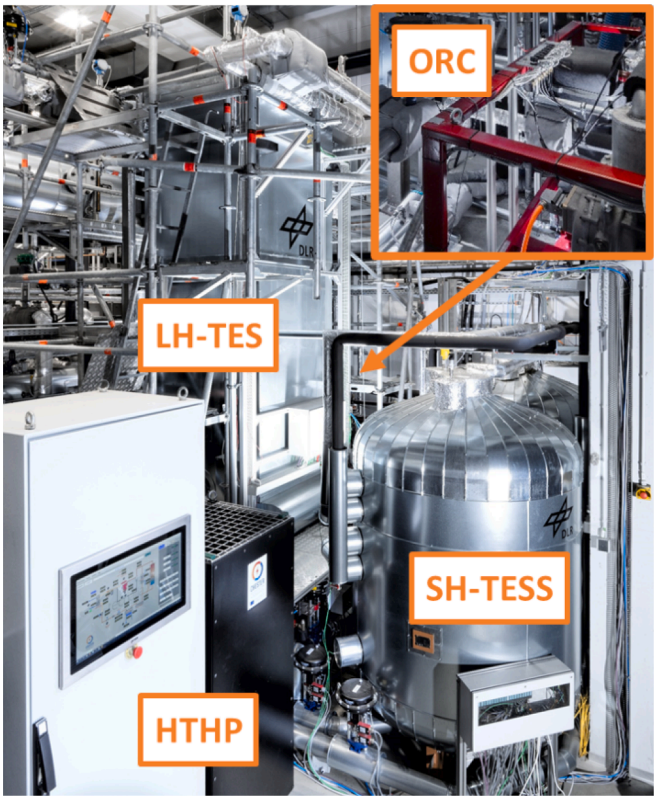

Fig. 3. CHESTER laboratory prototype. © DLR (CC BY-NC-ND 3.0).

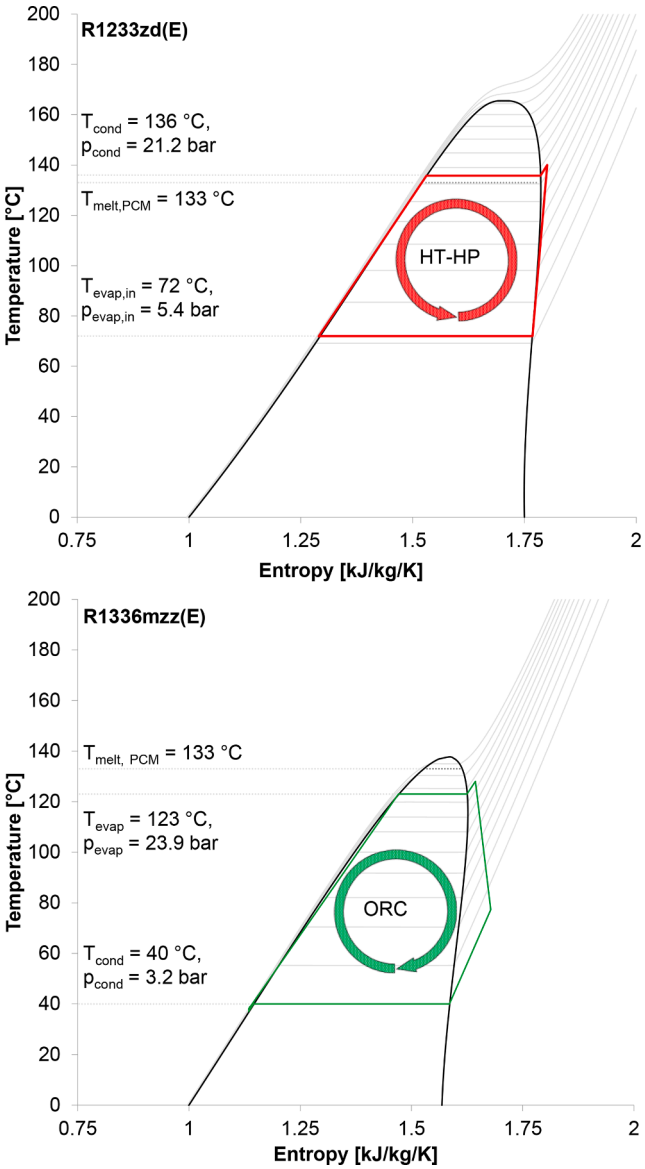

Fig. 4. T-s diagrams for the nominal heat upgrade and energy input (top) and energy dispatching (bottom) cycles of the CHESTER laboratory prototype.

2.3. High-temperature heat pump

For an optimal heat upgrade and energy input cycle in the CHESTER laboratory prototype, the HT-HP is designed by the research centre TECNALIA for heat source temperatures ranging from 60 to 100 °C, approximately, a design heat sink temperature above 133 °C and electrical consumption of 10 to 15 kW_{el}. A description of the detailed HT-HP design can be found in Hassan et al. [37] and the analysis of the first experiments for different operating conditions in Ramirez et al. [38]. Fig. 5 shows a simplified P&I diagram of the whole CHESTER laboratory prototype. The components of the HT-HP are shown on the left: a high-temperature compressor, the LH–TES serving as condenser, a subcooler connected to the SH–TES, an expansion valve and an evaporator connected to the heat source.

The high-temperature compressor is a single-piston reciprocating type model HBC511 manufactured by Viking Heat Engines (now Heaten AS). It is designed to operate under high-temperature conditions and is compatible with all common refrigerants of the 3rd and 4th generation. This includes R1233zd(E), although this had not been experimentally tested before this laboratory prototype [39]. The compressor speed can be varied between 600 and 1500 rpm for the regulation of the heating capacity of the HT-HP. The evaporator and the subcooler are commercially available brazed plate heat exchangers from the manufacturer SWEP, with 70 and 50 plates respectively. The nominal heating capacities for these are 46 and 23 kW_{th}. The control loop on the water side of the evaporator attempts to maintain a temperature difference of around 5 K between the water inlet and outlet temperature by varying the speed of the water pump. In the subcooler of the HT-HP, the pump of the cold water tank operates at a constant speed, while the flow rate required to achieve a water outlet temperature of approx. 120 to 130 °C under steady-state conditions is regulated with a 3-way valve. The expansion valve was selected based mainly on its compatibility with the refrigerant and the maximal allowable operating temperature. An algorithm for controlling the expansion valve was developed for the general control routine of the prototype, as the working conditions differ from the original working conditions of the manufacturer. The expansion valve is controlled to maintain a refrigerant superheating of around 10 K at the suction line of the compressor. In addition to these components, a suction line accumulator, an oil separator, a solenoid valve and pressure switches and valves are included within the circuit. The HT-HP control routine includes automatic start-up and shutdown routines and special subroutines for temperature control of the compressor cooling water circuit and lubrication temperature control. More detailed information about the HT-HP is given by Hassan et al. [37].

2.4. High-temperature thermal energy storage system

The HT-TESS, designed by DLR, is a combined system consisting of an LH-TES and an SH-TES (Fig. 5, centre). The boundary conditions for the heat upgrade and energy input process are defined by the thermal output and thermodynamic conditions of the refrigerant at the optimal operation point of the HT-HP with approx. heat flow rates of 30 kW_{th} for the LH-TES and 25 kW_{th} for the SH-TES. The energy dispatching process was matched to the requirements of the ORC with the approx. heat flow rates of 43 kW_{th} for the LH-TES and 72 kW_{th} for the SH-TES. The storage capacity of the HT-TESS was chosen to allow for a full charging and discharging cycle within one working day. Due to the transient effects in the phase change material (PCM) during charging and discharging, the numeric modelling of the HT-TESS was mainly focused on the LH-TES unit. For the detailed design of this component, a thermodynamic analysis of the internal heat exchanger and a parameter study to determine the required storage configuration was carried out similar to Johnson et al. [40]. To enable the use of different refrigerants and lubricants in the HT-HP and ORC circuits as well as tight requirements for the temperature gradients, the LH-TES was designed and built as a novel dual-tube finned tube (Fig. 6) vertical shell and tube type storage unit. With this innovative design, an uncontrolled transport of lubricants between HT-HP and ORC and thus a lack of lubrication can be avoided. The shell and tube type storage is considered one of the most popular devices for commercial and industrial applications in medium and high temperature thermal energy storage [41]. It is characterised by its simplicity, especially when the pressurised heat transfer fluid flows inside the tubes and the PCM in the shell is depressurised. In addition, the number and height of the heat exchanger tubes allow for easy scalability. The storage consists of two tube registers connected thermally and physically by an aluminium fin. To achieve a constant heat output

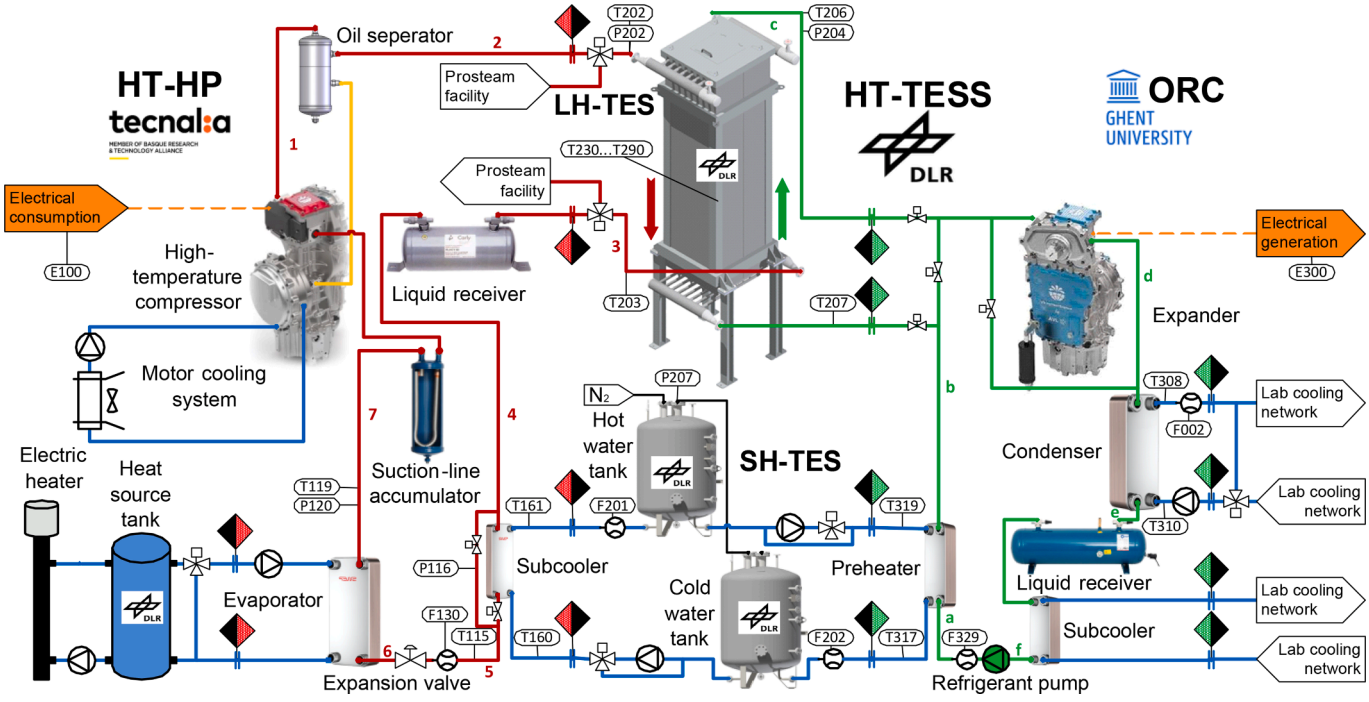

Fig. 5. Simplified P&I diagram of the CHESTER laboratory prototype.

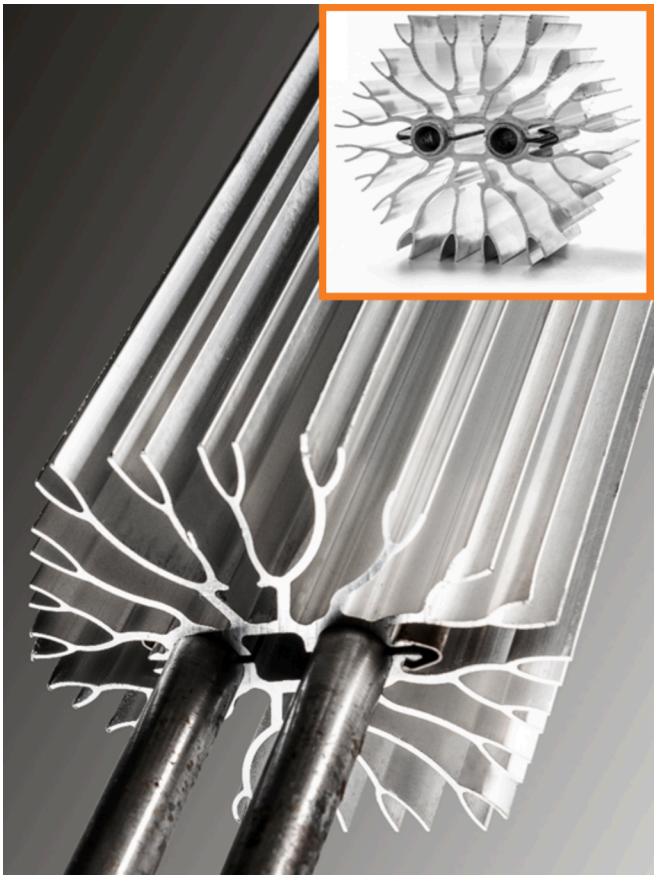

Fig. 6. Novel dual-tube finned tube design for the LH-TES. © DLR (CC BY-NC-ND 3.0).

while maintaining a low temperature difference between PCM and refrigerant, heat transfer structures made of extruded axial aluminium fins were developed in an iterative process with a manufacturer, taking techno-economic aspects into account. The extruded aluminium 6060 fin halves are attached to the tubes with 1.4310 spring steel clips. The fin-pair structure is hexagonal, allowing for an optimal packing density. For more information about the attachment method, see Johnson et al. [42].

In total, 56 finned-tube pairs are inserted in the storage container. The tubes in the tube registers each have an outer diameter of 17.3 mm and a wall thickness of 2.3 mm. The tube-pairs are aligned in rows of seven by eight. The rows of seven are connected to two subheader sets, each with an outer diameter of 42.4 mm and a wall thickness of 3.0 mm. The resulting eight pairs of subheaders are connected to two main headers, each with an outer diameter of 139.7 mm and a 4.0 mm wall thickness. The material used for the tubes and outer shell of the LH-TES is 16Mo3. The outer shell of the LH-TES is a rectangular containment with an inner volume of $1000 \times 1070 \times 3000$ mm^3. The total height of the LH-TES, including the base, is 4646.7 mm. The storage unit is filled with approx. 4450 kg of PCM. To investigate the temperature distribution in the LH–TES, 10 multipoint thermocouples with 6 measurement levels each (Fig. 5, T_{230} to T_{290}) were placed at different horizontal positions in the PCM, using the multipoints to provide a measurement at six heights. During the energy input cycle, charging the storage, the R1233zd(E) flows inside a tube register from the top to the bottom of the LH-TES, allowing the condensing refrigerant to flow according to gravity and the PCM on the shell side to melt and thermally expand at the top of the storage first. On the contrary, during the energy dispatching cycle, discharging the storage, the R1336mzz(E) flows inside the second tube register from the bottom to the top of the LH-TES. This allows the evaporating liquid with lower density to leave the LH-TES at the upper part, while the PCM on the shell side solidifies and thermally shrinks at the bottom of the storage first. In Fig. 5, a connection to another test infrastructure (Prosteam) can be seen on the HT-HP piping side. Prosteam is a refrigerant evaporation and condensation unit, currently also filled with R1233zd(E), that allows for the preconditioning of the LH-TES for the experiments with the CHESTER laboratory prototype. For the operation of the CHESTER laboratory prototype, preconditioning is required, as the HT-HP is not able to preheat the LH-TES from ambient temperatures due to the design-point temperature level. In real applications, direct preheating with a low-temperature heat source or with electrical resistance heaters could be used for this purpose.

The layout of the SH-TESS is based on the nominal point operation. Since the operation parameters in this component are almost constant during charging and discharging no transient simulation was required. The SH-TES is a closed pressurised loop with two water tanks, connected to both the subcooler and preheater of the HT-HP and ORC, respectively. In this loop, water is used as the heat transfer fluid under a nitrogen atmosphere of approx. 5 bar. A connection line between the tanks enables a pressure balance and sequential charging and discharging without mixing the hot and cold fluids. The system was designed for a charging and discharging time of about 4 h each. A schematic view of the SH-TES can be seen in Fig. 7. Each tank is designed as a pressure vessel with a maximum operating pressure of 6 bar, resulting in a water saturation temperature of 159 °C and a maximum fill volume of 1.9 m^3. For the initial start-up and preconditioning between experiments, each tank can be preconditioned with 9 kW_{el} immersion heaters as well as with internal heat exchangers with a cooling power of 15 kW_{th} that are connected to the lab cooling network. During the energy input cycle and charging of the SH-TES, water from the cold water tank is pumped via the subcooler of the HT-HP to the hot water tank. During the energy dispatching cycle and discharging of the SH-TES, hot water from the hot water tank is pumped via the preheater of the ORC to the cold water tank.

2.5. Organic Rankine cycle

The ORC is designed by the University of Ghent with a design power of 10 kW_{el} and is used to convert the heat stored in the HT-TESS to electricity and low temperature heat, thereby discharging the CHESTER laboratory prototype. The LH-TES serves as the evaporator for the refrigerant and the SH-TES as a preheater. The further components of the ORC are in Fig. 5 on the right: the expander, a pump and two further heat exchangers for the condenser and the subcooler.

The volumetric piston expander has an internally variable valve timing mechanism that can be used to control the internal expansion ratio. Having the flexibility to control the internal expansion ratio

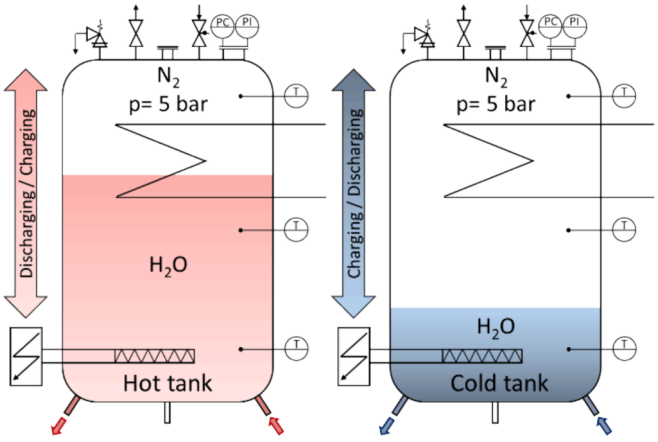

Fig. 7. Schematic view of the SH-TES.

Table 1
Overview of all measurement devices and their accuracy.

Parameter	Sensor	Accuracy
$T_{119}, T_{161}, T_{160}, T_{115}$	PT1000 RTD, 2-wire sheath sensor fixed in immersion sleeves	IEC 60751 Class B±(0.3 °C + 0.005 × T)
p_{116}, p_{120}	piezoresistive relative pressure sensor, (0…40 bar), (−1…15 bar)	1 % FS, ±400 mbar, ±150 mbar
$\dot{m}_{130}$	Coriolis mass flow meter	±(0.001 × $\dot{m}$)
$P_{100(H)}$	power measurement terminal + AC Current Transformer, (0…50 A), (0…500 V)	0.5 % FS, ±0.25 A, ±2.5 V
$T_{202}, T_{206}, T_{203}, T_{207}$	PT100 RTD, 4-wire spring fixed sheath sensor in immersion sleeves	1/10 Class B±(0.3 °C + 0.005 × T)/10
$T_{230} \cdots T_{290}$	Type K Multipoint-Sheath-Thermocouple	Class 1, ±1.5 °C
p_{202}, p_{204}	piezoresistive absolute pressure sensor, (0…40 bar)	0.05 % FS, ±20 mbar
p_{207}	piezoresistive absolute pressure sensor, (0…6 bar)	0.25 % FS, ±15 mbar
$\dot{m}_{201}, \dot{m}_{202}$,	Coriolis mass flow meter	±(0.001 × $\dot{m}$)
$T_{308}, T_{310}, T_{319}, T_{317}$	PT100 RTD, 3-wire inflow sheath sensor	IEC 60751 Class B±(0.3 °C + 0,005 × T)
$\dot{m}_{329}$	Coriolis mass flow meter	±(2.7 kg/h + 0.0015 × $\dot{m}$)
$\dot{V}_{002}$	magnetic inductive flow meter	±(0.005 × $\dot{V}$)
$P_{300(O)}$	control unit + smart line module + motor module	assumed negligible

directly improves the ability of the ORC to perform well under partial-load conditions and adapt the internal process conditions to the external process conditions of the HT–TESS. The rated electrical power output of the expander, as indicated by Viking Heat Engines (now Heaten AS), is 15.5 kW_{el} and can operate at a maximum inlet pressure and temperature of 30 bar and 215 °C. An automatic bypass valve is used to bypass the expander during start-up when the refrigerant is not within the design expander inlet conditions. The ORC power output can be modulated using the speed control of the expander and the pump. The refrigerant pump is a G10-X diaphragm pump from Wanner with a capacity of 30.6 l/min. The pump is capable of reaching pressures up to 69 bar at 1450 rpm and is connected to a 2.2 kW_{el} electric motor from WEG. A B400T brazed plate heat exchanger from SWEP with a nominal capacity of 120 kW_{th} and 120 plates is used as the condenser. The condenser is connected to a cooling water network, which enables temperature regulation. After the condenser, the refrigerant is directed to a liquid receiver and further cooled in the ORC subcooler, which is connected to the cooling water network and guarantees a completely liquified refrigerant at the pump inlet. The subcooler is a B28 brazed plate heat exchanger with 34 plates from SWEP. After the pump, the refrigerant is preheated in the preheater connected to the SH-TES. This is another brazed plate heat exchanger from SWEP, with a capacity of 120 kW_{th} and 120 plates as well. This is sized for operation as an evaporator during stand-alone testing of the ORC and is oversized for the CHESTER laboratory prototype, in which the LH-TES is the evaporator. The ORC is controlled using a Siemens PLC to communicate the desired setpoint to the setup components. More detailed information about the ORC is given by Couvreur et al. [43].

2.6. Measurement devices and accuracy

The simplified P&I diagram in Fig. 5 shows only the measuring points and valves relevant to the following analysis. Since it is derived from the detailed P&I diagram, the numbering is not consecutive. Table 1 lists all measuring sensors and measuring devices whose measured values were used for the data reduction with type designation, measuring principle and accuracy. Different measurement devices are used for each component of the CHESTER laboratory prototype, as the three subsystems were designed and built in different research institutes and partially use different measurement methods.

3. Methods

To test the CHESTER laboratory prototype, different experiments were carried out to investigate the performance of the overall system and the subsystems. To this end, parameter variations during the heat upgrade and energy dispatching processes enabled the characterisation of the three subsystems in interaction with each other, the investigation of their dynamic behaviour and the identification of optimal operating parameters. Due to the focus on the overall system in this publication, one experiment during the heat upgrade and energy input and one during the energy dispatching process are presented, each without additional manual parameter variation. Since the three subsystems were designed and constructed separately and used separate control systems and data acquisition, the data acquisition rate and clock times were dissimilar. For this reason, the data was summarized in an overall synchronization table after each test with a time discretization of 1 Hz.

3.1. Calculation method

For the calculation of the energy balance, most of the energy flow rates were determined on the water side of the heat exchangers, balancing the energy flowing into and out of the system; this analysis is most relevant for upscaling and future analyses. All fluid properties were calculated with REFPROP [36].

The heat flow rate $\dot{Q}$ can be calculated from the mass flow rate $\dot{m}$ and the enthalpy difference Δh. The water in this system is single-phase and, according to Gibbs' phase rule, two intensive state variables such as temperature T and pressure p are sufficient to determine the specific enthalpy h at a specific point.

On the refrigerant side, some parts of the circuits are two-phase, so the two measured state variables are not sufficient for the determination of the specific enthalpy. Since the LH-TES can only be balanced using the refrigerant, having refrigerant in a single phase at the inlet and outlet of the storage was aimed for. The refrigerant entered the LH-TES superheated during charging/condensation and subcooled during discharging/evaporation, each by about 5 to 10 K.

Starting with the heat upgrade and energy input cycle, which charges the system (C) the heat flow rates at the LH-TES (LH) and the subcooler heat exchanger at the SH-TES (SH) can be calculated by the Eq. (1) to (2):

$$\dot{Q}_{LH(C)} = \dot{m}_{130} * \left[h_{LH(C),out}(T_{203}, p_{202}) - h_{LH(C),in}(T_{202}, p_{202}) \right] \quad (1)$$

$$\dot{Q}_{SH(C)} = \dot{m}_{201} * \left[h_{SH(C),in}(T_{160}, p_{207}) - h_{SH(C),out}(T_{161}, p_{207}) \right] \quad (2)$$

The heat flow rate of the evaporator heat exchanger at the heat source (so) of the HT-HP is calculated from the refrigerant side, since the error analysis has shown that, especially for small temperature differences,

small measurement uncertainties in the temperature measurement on the water side of the heat source can cause significant errors in the calculated heat flow rate. Thus, a 1 K measurement error in the temperature measurement can cause an error in the heat flow rate of over 12 kW_{th}. In the balance of the refrigerant side, a temperature measurement error of 5 K can result in a maximum error of up to 3 kW_{th}. Since the refrigerant is in the two-phase state before entering the evaporator, an isenthalpic expansion within the expansion valve is assumed. Therefore, the enthalpy values before the expansion valve and after the evaporator are used for the calculation of the transferred thermal energy. The equation for the heat flow rate therefore reads as Eq. (3).

$$\dot{Q}_{so(C)} = \dot{m}_{130} * \left[h_{so(C),out}(T_{119}, p_{120}) - h_{so(C),in}(T_{115}, p_{116}) \right] \tag{3}$$

For the calculation of the electrical power of the compressor during the charging process $P_{co(C)}$ with the compressor speed n_{co}, the current and voltage are measured and permanently logged for each phase of the 3-phase engine.

For the energy dispatching process (D), the heat flow rates at the LH-TES, the preheater heat exchanger at the SH-TES and the heat sink (si) can be defined in Eq. (4) to (6):

$$\dot{Q}_{LH(D)} = (\dot{m}_{329} - \dot{m}_{off}) * \left[h_{LH(D),out}(T_{206}, p_{204}) - h_{LH(D)}(T_{207}, p_{204}) \right] \tag{4}$$

$$\dot{Q}_{SH(D)} = \dot{m}_{202} * \left[h_{SH(D),out}(T_{317}, p_{207}) - h_{SH(D),in}(T_{319}, p_{207}) \right] \tag{5}$$

$$\dot{Q}_{si(D)} = \left[\varrho_{002}(T_{308}, 100\ kPa) * \dot{V}_{002} \right] * \begin{bmatrix} h_{si(D),out}(T_{308}, 100\ kPa) \\ -h_{si(D),in}(T_{310}, 100\ kPa) \end{bmatrix} \tag{6}$$

The mass flow rate $\dot{m}$ of the LH-TES includes an offset $\dot{m}_{off}$ of 0.28 kg/s, which was set in the Coriolis mass flow meter. For the pressure on the water side of the heat sink, 100 kPa was assumed. As the magnetic-inductive flow meter, F308 measures the volumetric flow rate $\dot{V}$, the density ϱ was determined with the temperature and pressure to calculate the mass flow rate. Within the overall comparison of the energy flows, only the heat rejected in the condenser is considered useful. The heat rejected in the subcooler is considered heat loss due to the low temperature level. The electrical power of the expander during the discharging process $P_{ex(D)}$ is retrieved from the drive controlling the expander speed n_{ex} using the PLC. The power of the refrigerant pump $P_{pu(D)}$ and the pump speed n_{pu} are retrieved similarly. The drives themselves measure DC voltage and current.

The total transferred energy E during a certain period of time can be calculated by the integral of the heat flow rates and the electrical power. Since these data are logged every second, the transferred energy in kWh is calculated by

$$E_i = \frac{\sum_{j=0}^{j=i} \dot{Q}_j}{3600} \tag{7}$$

for every second j within the period of i seconds.

For a proper visualization of the experimental results, the logged data are smoothed with a moving average in a 10 s time window. This allows the results to be better analyzed by the viewer without losing data.

3.2. Key performance indicators

In literature, the roundtrip efficiency η_{RT} is determined based on steady-state thermodynamic cycle analysis or steady-state experimental testing. The roundtrip efficiency is commonly calculated as the product of the efficiencies: $COP_{(C)}$ for the heat upgrade and energy input cycle, $\eta_{(TESS)}$ for the HT-TESS and $\eta_{(D)}$ for the energy dispatching cycle. [10,17,26]

$$\eta_{RT} = COP_{(C)} \cdot \eta_{(TESS)} \cdot \eta_{(D)} \tag{8}$$

Since the experiments with the CHESTER laboratory prototype are transient processes, the arithmetic means, maxima and minima for the individual efficiencies were determined during time-limited quasi-stationary points of the whole measurement campaign. For the HT-HP, the quasi-stationary COP values were calculated using the time-averaged temperatures, pressures and mass flow rates of 10 min operating intervals in which no significant parameter fluctuations were observed. Between 8 and 9 quasi-stationary points were determined for each of the analysed experiments of the whole measurement campaign. For the ORC, the LH-TES outlet temperature of the refrigerant depends on the state of charge and is thus transient and not directly controllable. The quasi-stationary points were thus calculated by dividing this LH-TES outlet temperature in 2 °C intervals into periods where other inputs were kept the same. The quasi-stationary points correspond to the time-averaged value over the time interval corresponding with the 2 °C temperature interval.

The ratio of supplied electrical power to useful electrical power ε is an important parameter to characterise an energy management system for converting and storing electrical energy. The calculation of the net power ratio ε_{net} includes the electrical power fed into the compressor as well as the parasitic power of the pump and reads:

$$\varepsilon_{net} = \frac{\sum E_{el(D)}}{\sum E_{el(C)}} = \frac{\left|E_{el,ex(D)}\right| - \left|E_{el,pu(D)}\right|}{\left|E_{el,co(C)}\right|} \tag{9}$$

This calculation does not consider the transient phases of the experiments as well as different setpoints or states of charge so these will influence the net power ratio. As the charging and discharging periods are not the same length of time, the electrical energy is used for the calculation instead of the average power.

The overall roundtrip utilization rate η_{net} is the ratio of the net energy produced during the energy dispatching process to the energy sum needed during the heat upgrade and energy input process and is defined as:

$$\eta_{net} = \frac{\sum E_{(D)}}{\sum E_{(C)}} \tag{10}$$

The evaluation of roundtrip efficiency in CHEST systems was discussed by Jockenhöfer et al. [24]. The definitions apply to simultaneous energy input and dispatching processes. Therefore, the calculations are adapted for separate subsystem operations to

$$\sum E_{(D)} = \left|E_{el,ex(D)}\right| + \left|E_{th,si(D)}\right| - \left|E_{el,pu(D)}\right| \tag{11}$$

$$\sum E_{(C)} = \left|E_{el,co(C)}\right| + \left|E_{th,so(C)}\right| \tag{12}$$

where the energy provided during the energy dispatching process $E_{(D)}$ is the sum of the energy transferred by the expander and converted by the generator into electricity, the thermal energy transferred to the heat sink, and the energy consumption of the refrigerant pump. The energy transferred to the subcooler of the ORC is considered not useful. The energy required during the heat upgrade and energy input process $E_{(C)}$ is similarly a sum of the consumption by the compressor and the thermal energy transferred from the heat source.

4. Experimental results and discussion

Table 2 gives an overview of the initial conditions of the presented experiments. The heat upgrade and energy input process by the HT-HP presented here starts after a previous energy dispatching process of the CHESTER laboratory prototype by the ORC so that the initial conditions of the HT-TESS result from the final conditions of the previous storage discharging. The mean PCM temperature of the LH–TES $\overline{T_{LH}}$, is calculated with 54 temperature measurements of the multipoint thermocouples. The fill level of the SH-TES hot water tank $L_{ht(SH)}$ with the water

Table 2
Experimental initial conditions and target operating parameters.

Heat upgrade and energy input	
$\overline{T_{LH}}$	≈120.0 °C
$L_{ht(SH)}$	≈0.8 *m*
$T_{ht(SH)}$	≈130.4 °C
$L_{ct(SH)}$	≈1.0 m
$T_{ct(SH)}$	≈27.7 °C
T_{so}	≈95.0 °C
$\dot{m}_{130}$	≈0.3 kg/s
n_{co}	≈1500 rpm
Energy dispatching process	
$\overline{T_{LH}}$	≈136.7 °C
$L_{ht(SH)}$	≈1.6 m
$T_{ht(SH)}$	≈119.3 °C
T_{si}	≈25.0 °C
$\dot{m}_{329}$	≈0.4 kg/s
n_{ex}	≈1000 rpm
valve position ex.	≈170°

temperature $T_{ht(SH)}$ and the fill level of the cold water tank $L_{ct(SH)}$ with the water temperature $T_{ct(SH)}$ also results from the previous storage discharging. The water temperature of the heat source T_{so} was set to 95.0 °C, resulting in an average water inlet temperature of approx. 92 °C into the heat exchanger. For the refrigerant mass flow rate $\dot{m}_{130}$ and the compressor speed n_{co}, the target values are given.

The energy dispatching process by the ORC starts after preconditioning the LH–TES with Prosteam and the SH-TES with the immersion heaters. The SH-TES hot water tank is completely filled, therefore the values for the cold water tank are not included. The temperature of the heat sink T_{si} is given by the DLR cooling water network temperature. The ORC expander valve position for this experiment was set to 170° resulting in a full load expander capacity.

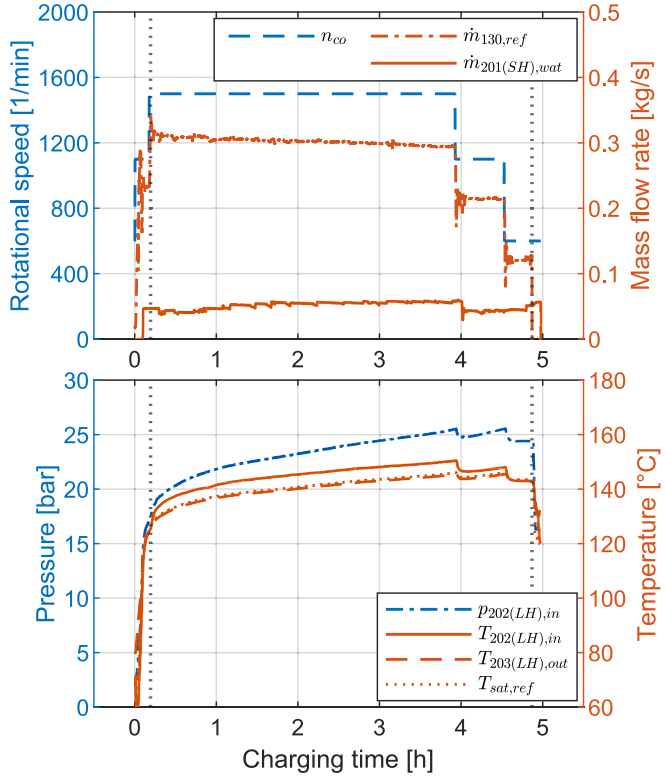

Fig. 8. Compressor speed and mass flow rate (top) and temperature and pressure at LH-TES (bottom), plotted over the heat upgrade and storage charging time.

4.1. Heat upgrade and energy input process

To describe the heat upgrade and energy input process, Fig. 8, top, shows the target compressor speed and the measured water mass flow rate from the cold to the hot water tank of the SH-TES (wat) as well as the measured refrigerant mass flow rate (ref). Fig. 8, bottom, shows the measured refrigerant pressure at the LH-TES inlet with the corresponding saturation temperature (sat) and the measured temperatures at the LH–TES inlet and outlet. All values are plotted over the operating time. The ramp-up of the heat upgrade and energy input process started with turning on the water pump of the evaporator of the HT-HP at 0 h, followed by the water pump of the SH-TES. Water flowed from the cold water tank through the subcooler of the HT-HP to the hot water tank at a relatively constant mass flow rate of approx. 0.05 kg/s. During the nominal operation stage, which is within the time period marked by the dotted vertical lines, the rotational speed of the compressor was set at 1500 rpm, resulting in a refrigerant mass flow rate of approx. 0.3 kg/s. As can be seen, the inlet pressure of the LH-TES rises progressively until approx. 25 bar at 3.9 h, corresponding to a saturation temperature of the refrigerant of 144.9 C. At the outlet, the temperature of the refrigerant corresponds to the saturation temperature; for the evaluation, it is assumed that the refrigerant leaves the LH-TES saturated. With the increasing state of charge of the LH-TES, heat transfer decreases and the pressure on the high-pressure side increases. Therefore, pressure has proven to be a good indicator for implementation in the ramp-down strategy of the control system. The compressor speed is reduced from 1500 to 1100 rpm as soon as the pressure on the high-pressure side exceeds 25 bar for more than 1 min, which results in a pressure reduction of about 1 to 2 bar. If the pressure rises above 25 bar again for more than 1 min, the compressor speed is reduced to 600 rpm and, in the last step, the HT-HP is switched off after approx. 5 h. The nominal operation stage between the two dotted lines is approx. 4.7 h.

Fig. 9 displays the temperature distribution in the PCM of the LH-TES and the fill level of the hot water tank during the heat upgrade process and therefore storage charging time. The PCM temperature arithmetic and median values at the beginning of the charging process are both around 120.0 °C, resulting in a symmetrical temperature distribution. Nevertheless, the spread is relatively large with a minimum value of 112.2 °C and a maximum value of 129.9 °C, which on the one hand indicates a quick previous discharge of the LH-TES and on the other hand poor heat transfer through the solid PCM. During the heat upgrade process and storage charging, the spread decreases, which is because of the increasing liquid fraction of the PCM with a better heat transfer with

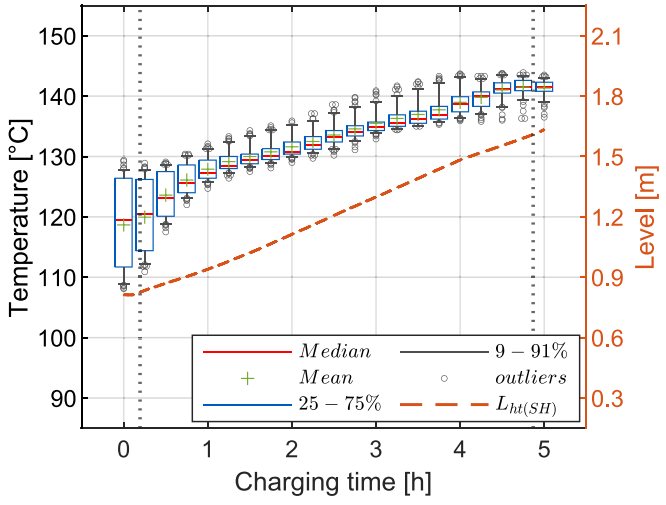

Fig. 9. Temperature distribution of the PCM in the LH-TES and fill level of the SH-TES hot water tank during the heat upgrade process and storage charging time.

natural convection. Furthermore, the small temperature difference between the LH-TES inlet and outlet temperature of the refrigerant (Fig. 8, bottom) indicates a large condensation zone, which further homogenises the temperature differences over the storage height. At the same time, a slight shift of the symmetry towards higher temperature values can be seen, so that the mean value is above the median. This trend is typical for the charging process and is caused by the higher temperatures in the vicinity of the LH-TES refrigerant tubes. The PCM temperature arithmetic and median values at the end of the charging process are 141.5 °C with a minimum value of 139.3 °C. As both temperatures are above the PCM melting range, the LH-TES can therefore be assumed to be fully charged. The level of the SH-TES hot water tank increases almost linearly to a complete fill at 1.6 m with an end water temperature of 125.3 °C.

4.2. Energy dispatching process

The energy dispatching process with the target expander- and pump speed, the measured water mass flow rate from the hot to the cold water tank of the SH-TES and the measured refrigerant mass flow rate can be seen in Fig. 10. As given by Table 2, the level of the full SH-TES hot water tank is 1.6 m with a preconditioned water temperature of 119.3 °C, which corresponds approximately to the final conditions of the discharging described previously. Again, the measured refrigerant pressure with the corresponding saturation temperature at the LH-TES inlet and the measured temperatures at the LH-TES inlet and outlet are shown in the bottom graph. The ramp-up of the energy dispatching process started with turning on the SH-TES pump at 0 h, followed 10 min later by the refrigerant pump to preheat the system, bypassing the expander and the LH-TES. Water flowed from the hot water tank through the preheater of the ORC to the cold water tank at a relatively high mass flow rate of approx. 0.16 kg/s in comparison to the nominal operation stage with 0.10 kg/s. The inlet and outlet temperatures of the LH-TES rise at 0.3 h when the bypass of the LH-TES is closed so that all refrigerant flows through the LH-TES. The LH-TES outlet temperature reaches values up to 132.4 °C and the inlet temperature up to 111.5 °C, continuing preheating the ORC for further 10 min. After preheating the ORC, the expander was brought up to 500 rpm with externally supplied electricity. By closing the bypass valve of the expander, the expander switches from engine mode to generation mode and feeds electricity into the grid. The expander speed was then set to the target value of 1000 rpm, thus initiating the start of the nominal operating stage. The pressure begins to rise to a value of 14.0 bar, just after the expander bypass has been closed. The refrigerant pump set value of 800 rpm during the nominal operation stage results in a refrigerant mass flow rate of approx. 0.37 kg/s, including offset. The water mass flow rate in the preheater has been gradually adjusted after the start of the nominal operation from 0.16 kg/s to 0.10 kg/s to adjust the refrigerant inlet temperature around 5 K below the refrigerant saturation temperature so that the refrigerant enters the LH-TES in a subcooled state. The LH-TES inlet temperature during nominal operation is therefore between 93 °C and 90 °C. During the nominal operational stage, the pressure decreases slightly from a value of 14.6 bar to a value of 13.6 bar, corresponding to refrigerant saturation temperatures of 98.8 °C and 95.6 °C, respectively. The LH-TES inlet temperature levels during the nominal operation stage show a high correlation to the water mass flow rate of the preheater. The outlet temperature decreases during the nominal operation stage from 127 °C to 102.7 °C, corresponding to a decreasing refrigerant superheat of around 28 K to 7 K. For the ORC, the superheat was chosen as an indicator to terminate the experiment. A minimum overheating of 5 K should be maintained to avoid liquid drops in the expander. Furthermore, the water level of the SH-TES hot water tank is also a significant indicator for finishing the experiment. To ramp down the ORC, the expander and refrigerant pump speed was gradually reduced simultaneously until the ORC was switched off after approx. 3.6 h. The nominal operation stage between the two dotted lines is approx. 2.9 h.

Fig. 11 shows the energy dispatching process, again with the temperature distribution in the PCM of the LH-TES and the fill level of the hot water tank. The mean and median values at the beginning of the discharging process are both around 136.7 °C, showing a symmetrical temperature distribution. This value is 4.8 K lower than the end mean value of the storage charging, but still above the melting range of the PCM, so it can be assumed that this temperature difference is due to partial storage of sensible heat. Compared to the storage charging with the HT-HP, the spread at the beginning is very low, so an almost homogeneous temperature distribution in the LH-TES can be assumed.

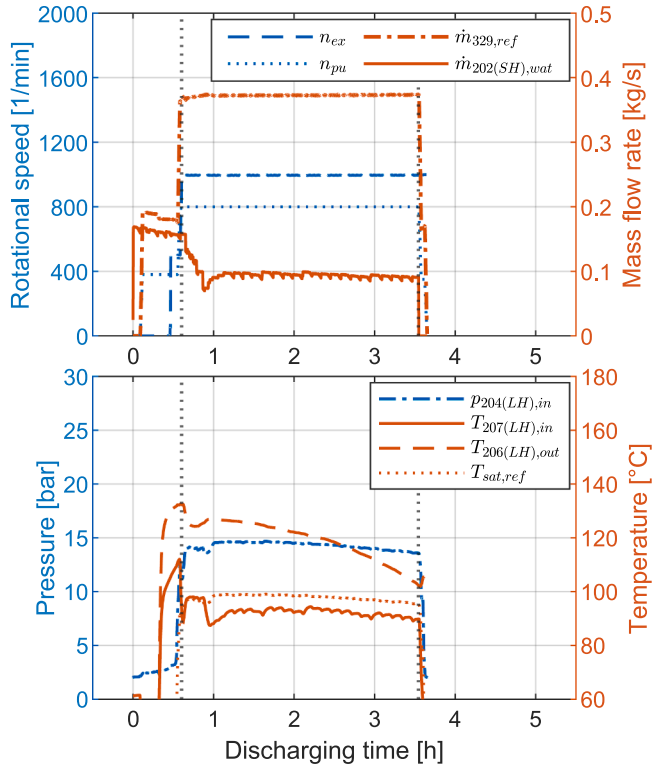

Fig. 10. Expander speed, pump speed and mass flow rate (top), temperature and pressure at LH-TES (bottom), plotted during the energy dispatching process and storage discharging time.

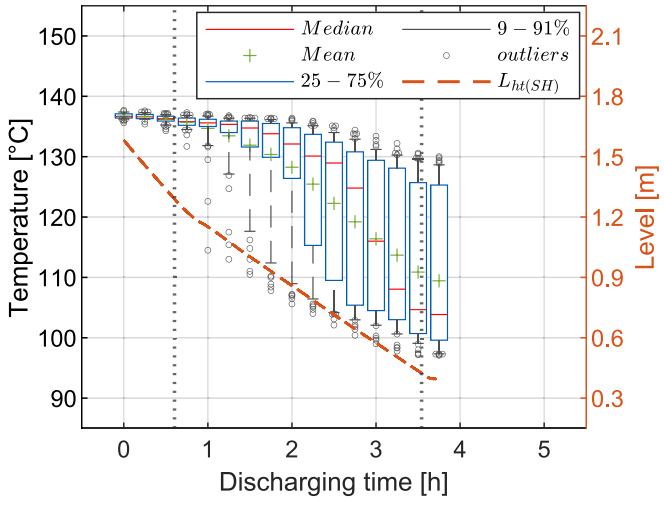

Fig. 11. Temperature distribution of the PCM in the LH-TES and fill level of the SH-TES hot water tank during the energy dispatch process and storage discharging time.

During the storage discharging, the spread increases, which is on the one hand due to the reverse effect of the charging process. The increasing solid fraction of the PCM results in poorer heat transfer due to a reduction in natural convection. On the other hand, the high temperature difference between the LH-TES inlet and outlet temperature of the refrigerant (Fig. 10, bottom) indicates a small evaporation zone, which further increases the temperature differences over the storage height and therefore the temperature spread.

Another influence could be the shorter nominal operation time for storage discharging compared to charging, with a difference of 1.7 h. After one hour of discharge, it can be seen that the symmetry of the distribution decreases, with the median taking on higher values than the mean. Here, the majority of the sensors measure higher temperatures, but the mean value is reduced to lower values, due to the drop in the minimum temperatures, measured in the bottom of the LH-TES. The asymmetry inverts after about 3 h of ORC operation, with the majority of the temperature values being lower than the mean. At this time, a major fraction of the PCM has already solidified and the refrigerant superheating occurs at the upper part of the LH-TES. The median and arithmetic mean values at the end of the discharging process are 103.5 and 109.2 °C, respectively, and the maximum value is 128.6 °C. As both temperatures are under the PCM melting range, the LH–TES can therefore be assumed to be fully discharged. The difference between the median and arithmetic mean values at the beginning of the charging process is 16.5 and 10.8 K respectively. The fill level of the SH-TES hot water tank decreases almost linearly, with a kink that displays the switchover of the water mass flow rate until it is empty at 0.4 m. At the same time, the fill level of the cold water tank is 1.37 m, with a water temperature of 24.9 °C.

4.3. Thermal and electrical performance

To evaluate the performance of the CHESTER laboratory prototype, the heat flow rate and electrical power were calculated based on the measured values. Fig. 12 shows the results obtained for the heat upgrade and energy input process. During the ramp-up stage of the heat upgrade cycle, it is observed that the heat absorbed from the heat source is mainly used for the preheating of the HT-HP itself, while only a minimum amount of heat is transferred to the LH-TES. In the nominal operation stage, the HT-HP absorbs around 50 kW_{th} from the heat source, supplying around 30 kW_{th} and 20 kW_{th} to the LH-TES and SH-TES, respectively, with an approximate electrical power consumption of 12 kW_{el} and heat losses of around 10 kW_{th}. During the ramp-down stage, when the HT-HP control system progressively reduces the compressor speed, it is visible that the heat flow rate of the system reduces accordingly, as well as the HT-HP power consumption, which reduces first to approx. 8 kW_{el}, and finally to 5 kW_{el} before the final shut-down of the system.

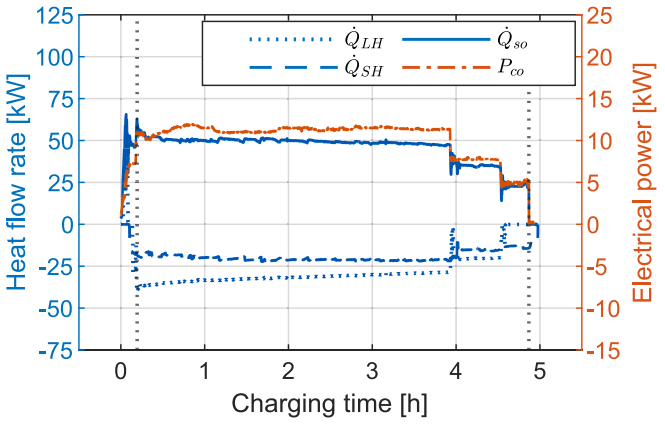

Fig. 12. Heat flow rate and electrical power plotted over the heat upgrade and energy input process and therefore storage charging time.

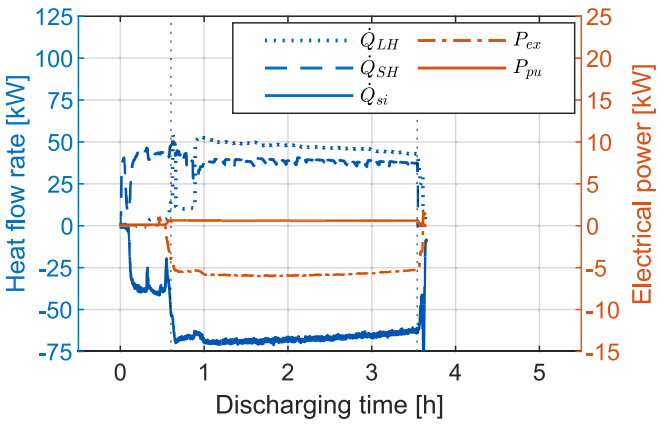

Fig. 13. Heat flow rate and electrical power plotted over the energy dispatching process and storage discharging time.

The performance results for the energy dispatching process are shown in Fig. 13. During the ramp up of the energy dispatching cycle, it can be observed that a heat flow rate of about 44 kW_{th}, absorbed from the SH-TES, was used for preheating the ORC, while a large amount of heat is being transferred to the heat sink with a heat flow rate of about 40 kW_{th}.

At the beginning of the nominal operation stage, the heat flow rate of the LH-TES increases to a value of up to 54 kW_{th} for about 2 min, decreasing to a value of approx. 10 kW_{th} for another 14 min, and then increases again to a value of approx. 53 kW_{th}. During this time period, the SH-TES water mass flow rate is decreased from 0.16 kg/s to 0.10 kg/s to adjust the refrigerant inlet temperature at the LH–TES. When the heat flow rate at the LH-TES amounts to 10 kW_{th}, the refrigerant inlet temperature is above the saturation temperature (Fig. 10), resulting in partial evaporation within the preheater. Since the electrical power of the expander only changes from 5.5 kW_{el} to 6.0 kW_{el} during this time period, this range is nevertheless assigned to nominal operation. Over the entire further energy dispatching time, the heat flow rate at the LH-TES decreases continuously until it reaches a value of approx. 43 kW_{th}, resulting in continuously decreasing outlet temperatures. The heat flow rate of the SH-TES, on the other hand, remains nearly constant over the entire nominal operating stage, with a value of approx. 39 kW_{th}. The electrical power production of the expander in the nominal operation stage is up to 6 kW_{el}, while the pump has a power consumption of approx. 0.6 kW_{el}.

4.4. Energy balance

The transferred energies during the operation of the CHESTER laboratory prototype can be calculated according to Eq. (7) with the previously mentioned heat flow rates and the electrical powers, as well as the duration of the nominal operation stage. Table 3 contains the

Table 3
Transferred energies during the charging and discharging processes.

	Unit	Heat upgrade	Energy dispatching
Heat source	[kWh_{th}]	214.1	–
Heat sink	[kWh_{th}]	–	−196.4
Compressor	[kWh_{el}]	48.5	–
Expander	[kWh_{el}]	–	−16.8
Pump	[kWh_{el}]	–	1.8
LH-TES	[kWh_{th}]	−131.5	129.8
SH-TES	[kWh_{th}]	−91.1	112.9
Balance	[kWh]	40.0	31.3
Relative balance	[%]	15.2	12.8
Duration	[h]	4.67	2.94
Heat losses	[kW_{th}]	8.6	10.6

transferred energies for the heat upgrade and energy input as well as energy dispatching cycles. When comparing these cycles, it can be seen that the transferred thermal energy of the heat source is about 10 % higher than the transferred thermal energy of the heat sink. It is important to note that the heat rejection in the subcooler is not considered thermal energy in the heat sink and is thus included in the heat losses. The transferred thermal energies at the LH-TES are almost the same, whereas those at the SH-TES are about 19 % lower for the heat upgrade and energy input cycle, due to the reduced water circulation in the SH-TES. The maximum capacity of a full SH-TES hot water tank is calculated to approx. 180 kWh_{th}, and of the full LH-TES to approx. 160 kWh_{th}. The electrical power consumed by the refrigerant pump is about 11 % of the electrical power generated by the expander. Comparing the energy inputs and outputs of the conversion cycles, their energy balance can be determined. This balance, representing the losses, can be normalized with the energy input to the cycle to get a more general impression of the total losses. The losses thus account for approx. 15.2 and 12.8 %during the heat upgrade and energy input process and energy dispatching process respectively. Using the heat balance and the duration of the nominal operation stage, the heat losses for each of the two subsystems result in about 10kW_{th}.

4.5. Thermodynamic cycles

With the pressure and temperature values of the refrigerants measured at specific points during the experiments, the entropy is calculated using REFPROP [36]. Subsequently, the different states can be plotted on the T-s diagrams as shown in Fig. 14 with numbers for the HT-HP and Fig. 15 with letters for the ORC. Additionally, the numbers and letters for the different states are included in Fig. 5. The data used were measured after an operation time of 2 h for both.

During the heat upgrade and energy input process, the refrigerant leaves the compressor in the gaseous state with a temperature of 148.4 °C and a pressure of 24.4 bar (1) and enters the LH-TES with a decreased temperature of 145.9 °C and a pressure of 23.5 bar (2). The refrigerant condenses in the LH-TES at a temperature of 141.4 °C, which is above the designed theoretical condensation temperature of 136 °C, and leaves the LH-TES in the liquid state at a temperature of 140.8 °C, ≈0.6 K below its condensation temperature (3). The refrigerant enters the subcooler at point 4 with a measured temperature of 119.8 °C and a pressure of 23.6 bar. The temperature drop between point 3 and point 4 can be explained by heat losses as a result of insufficient thermal insulation. The refrigerant is cooled down to 84.0 °C (5) in the subcooler and transfers the thermal energy to the water in the SH-TES. An isenthalpic process is assumed for the expansion valve to calculate the entropy in the two-phase region, resulting in a temperature of 81.3 °C at a pressure of 6.8 bar (6). In the evaporator, the temperature increases from 81.3 °C to 90.1 °C. Thereby, 81.3 °C corresponds to the saturation temperature at the evaporator inlet at 6.8 bar. Friction losses result in a pressure decrease at the evaporator outlet to 6.6 bar so that the evaporation temperature decreases to 79.8 °C. Thus, the refrigerant is overheated by 10.3 K after leaving the evaporator.

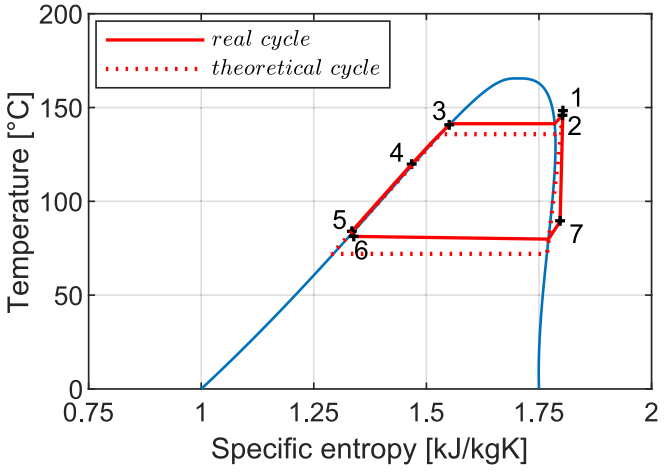

Fig. 14. Comparison of the real to the theoretical thermodynamic heat upgrade and energy input cycle, using values after 2 h of operation.

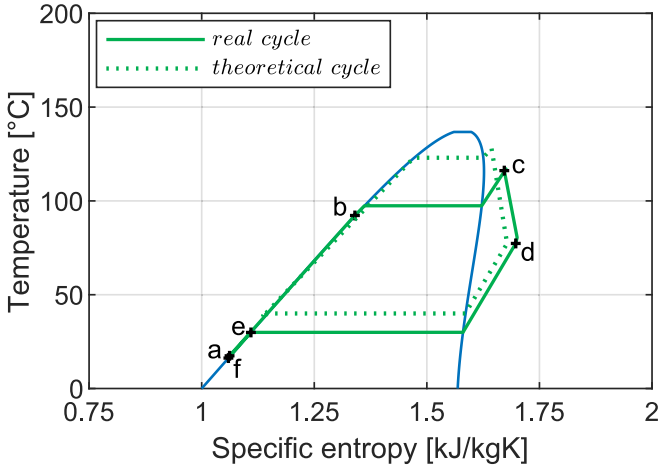

Fig. 15. Comparison of the real to the theoretical thermodynamic energy dispatching cycle, using values after 2 h of operation.

Comparing the theoretically calculated states with the measured data in the T-s diagram, thermodynamic optimization strategies can be derived to increase the efficiency of the CHESTER system. Thereby, the transferred energy into the SH-TES is limited by thermal losses between point 3 and point 4 and might be further reduced to values below the temperature of point 5. To avoid compressor damage, the refrigerant has to leave the evaporator in a gaseous state. Therefore, a certain superheating of the refrigerant within the evaporator must be ensured (7).

During the energy dispatching process, the refrigerant enters the preheater at a temperature of 17.4 °C and a pressure of 14.6 bar (a). The refrigerant flows through the preheater and thermal energy from the water in the SH-TES is transferred to the refrigerant and increases the refrigerant temperature to 92.2 °C (b), which is just below the evaporation temperature of 97.4 °C. Afterwards, the refrigerant is evaporated and superheated in the LH-TES to a temperature of 117.1 °C (c) and a measured pressure of 14.2 bar. In the expander, the refrigerant is expanded to 2.5 bar at a temperature of 80.5 °C (d). To close the refrigerant circuit, the refrigerant is cooled and condensed in the condenser, transferring the thermal energy to the heat sink. The refrigerant leaves the condenser with a temperature just below the condensation temperature of 29.9 °C, at a pressure of 2.3 bar (e). To ensure complete liquefaction of the refrigerant in the pump, the refrigerant passes through the subcooler that cools the refrigerant to 16.2 °C at a pressure of 2.2 bar (f). In the last step, the pump increases the pressure of the refrigerant to 14.6 bar.p.

Comparing the theoretical T-s diagram with the real measured one, one notes that the evaporation temperature of the real cycle is below the theoretical value of 123 °C at 23.9 bar. Since superheating of the gaseous refrigerant must be ensured to avoid damage from liquid droplets in the expander, the evaporation pressure and temperature were lowered. In addition, the condensation temperature is below the theoretical value of 40 °C at 3.2 bar. Further efficiency improvements could be achieved with a controllable subcooler to ensure fully liquefied refrigerant in the refrigerant pump with a minimum temperature drop.

4.6. Roundtrip efficiency, net power ratio and roundtrip utilization rate

The roundtrip efficiencies of the whole experimental campaign are

Table 4
Efficiencies at quasi-steady points during the whole experimental campaign with the CHESTER laboratory prototype.

	mean	max.	min.
Heat upgrade $COP_{(C)}$	4.97	5.62	3.69
Storage $\eta_{(TESS)}$	99.2 %	99.4 %	99.0 %
Energy dispatching $\eta_{(D)}$	6.2 %	6.7 %	5.0 %
Roundtrip η_{RT}	30.7 %	37.4 %	18.4 %

listed in Table 4. For the heat upgrade and energy input process, the *COP* depends mainly on the operating conditions: heat source temperature, heat sink (HT-TESS) temperature and refrigerant mass flow rate and compressor speed, respectively. For the HT-TESS, the efficiency in heat transfer is included in the efficiency of the charging and discharging process; the efficiency within the system is therefore defined by heat losses, which are temperature dependent. As the HT-TESS is a dynamic system with changing temperatures during operation, this is also time dependent. The heat losses were calculated to be between 1.5 and 2.6 kW_{th} for the LH-TES, depending on the state of charge, and around 1.3 kW_{th} for the SH-TES. For the energy dispatching process, the efficiency depends mainly on the operating conditions: heat source (HT-TESS) temperature, heat sink temperature, refrigerant mass flow rate, expander speed, and expander valve position.

The calculated total system roundtrip efficiencies are in the range of 18.4 % to 37.4 %. The overall efficiency is composed of the individual efficiencies of the subsystems at different operating points and therefore does not reflect the efficiency of one full-cycle experiment, but the generally achievable efficiency of the CHESTER laboratory prototype. As the efficiency of the storage system is time-dependent due to heat losses, the roundtrip efficiency of the overall system will decline with the passive storage times of the HT-TESS. To this end, the storage efficiency is shown in Fig. 16 over time, simplifying the heat losses to be linear during the passive storage phase.

The net power ratio and the roundtrip utilization rate are calculated according to the method described in section 3.2. With the transferred energies of 16.8 kWh_{el} for the expander, 1.8 kWh_{el} for the refrigerant pump and 48.5 kWh_{el} for the compressor, the net power ratio is 30.9 %. With the transferred energies used for the net power ratio calculation, 214.1 kWh_{th} for the heat source and 196.4 kWh_{th} for the heat sink, the overall roundtrip utilization rate is 80.5 %.

Although the initial and final states between the heat upgrade and energy input and energy dispatching processes of the presented experiments do not match exactly, the calculated net power ratio and roundtrip utilisation rate nevertheless can be used to show the potential and proof of the CHEST concept. Furthermore, in this publication, the outlet temperature of the water at the heat sink of the ORC with 32 °C is considered useful energy for the calculation of the roundtrip efficiency. For future experiments, a higher outlet temperature of about 40 °C must be aimed for (Fig. 1).

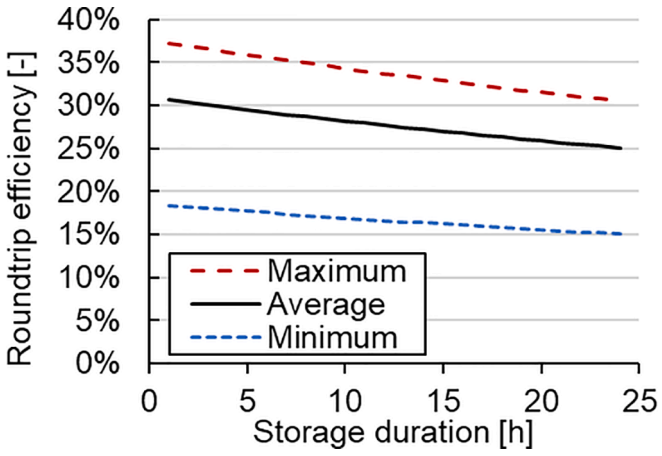

Fig. 16. Time-dependent expected roundtrip efficiency of the CHESTER laboratory prototype.

The key performance indicators shown here are limited on the one hand by the output of the ORC, which in turn is limited by the maximum temperature of the HT-HP. The advent of HT-HP which allows higher heat sink temperatures promises higher system efficiencies as stated in Steinmann [22]. On the other hand, the investigated prototype was still able to achieve the shown key performance indicators in real operation without any optimisation of the overall system and more importantly demonstrate the stable operation of the three innovative subsystems as part of a single energy management system. The efficiencies of the individual subsystems could be increased through better thermal insulation and optimisation of the components based on the gained experience and technical developments. In this context, the use of an isobaric engine pump instead of the electrical refrigerant pump in ORC is being investigated [44]. This could increase the electrical performance of the ORC by avoiding the power consumption of the electrical refrigerant pump. If the heat source can be used directly to operate the isobaric engine pump, the net power ratio can be increased by 3.7 % in the investigated scenario.

5. Conclusion and outlook

Thermally integrated pumped thermal energy storage systems are considered an appropriate technology for large-scale applications. Although numerous theoretical studies have investigated the potential of this storage technology in terms of efficiency and flexibility by coupling the electricity and heating sectors, the feasibility of this concept has not yet been proven experimentally. To overcome this gap the world's first CHESTER (Compressed Heat Energy Storage for Energy from Renewable Sources) laboratory prototype was designed and built at a representative scale. The operation of the CHESTER laboratory prototype confirms the feasibility of the thus far theoretical concept and provides information about the interaction of the three innovative subsystems HT-HP, HT-TESS and ORC.

The operating results and system performance were presented with representative experiments. The stable operation of a fully integrated CHEST system on a 10 kW scale was demonstrated and the stable function of the latent heat thermal energy storage as both a condenser and an evaporator was confirmed. As expected for such a laboratory prototype the overall roundtrip efficiency is still rather low, varying between 18 and 37 %. Taking the heat integration into account and combining the two presented experiments roundtrip utilization rate of 81 % could be achieved.

Future work focuses on improving the performance of the individual components, and increasing the maximum storage temperature, as detailed in the discussion section. Additionally, also the operation of the system as a flexible energy management system, with varying heat and power supply, will be investigated both from a technical as well as a techno-economic perspective. Further development of HT-HP towards higher temperatures is essential to enable the selection of a PCM with higher melting temperatures and thus reduced costs. Likewise, a reversible thermodynamic cycle instead of a separate HT-HP and ORC process could reduce costs and complexity.

CRediT authorship contribution statement

K. Theologou: Writing – original draft, Visualization, Validation, Methodology, Investigation, Formal analysis, Conceptualization. **M. Johnson:** Writing – review & editing, Project administration, Methodology, Investigation, Conceptualization. **J. Tombrink:** Writing – review

& editing, Visualization, Validation, Methodology, Investigation, Data curation, Conceptualization. **José L. Corrales Ciganda:** Data curation, Investigation, Writing – review & editing. **Felipe T. Trebilcock:** Data curation, Investigation, Methodology, Software, Validation, Writing – review & editing. **K. Couvreur:** Formal analysis, Investigation, Writing – review & editing. **R. Tassenoy:** Formal analysis, Investigation, Writing – review & editing. **S. Lecompte:** Conceptualization, Funding acquisition, Investigation, Project administration, Resources, Supervision, Writing – review & editing.

Declaration of competing interest

The authors declare that they have no known competing financial interests or personal relationships that could have appeared to influence the work reported in this paper.

Data availability

The data that has been used is confidential.

Acknowledgements

The work presented in this paper is a result of research activities of the CHESTER Project (www.chester-project.eu) which has received funding from the European Union's Horizon 2020 research and innovation programme under grant agreement No 764042.

References

[1] European Commission, (2018), "A Clean Planet for all - A European strategic long-term vision for a prosperous, modern, competitive and climate neutral economy", *52018DC0773, vol. 773*.
[2] Somosi S, Megyeri E. A Moving Target: Changing Priorities in the Energy Policy of the European Union. Int J Energy Econ Policy 2022;12(4):542–52. https://doi.org/10.32479/ijeep.13052.
[3] Martinot E. Grid Integration of Renewable Energy: Flexibility, Innovation, and Experience. Annu Rev Env Resour 2016;41(1):223–51. https://doi.org/10.1146/annurev-environ-110615-085725.
[4] European Environment Agency (EEA), (2023), "Decarbonising heating and cooling - a climate imperative", *Briefing no. 27/2022,* doi: 10.2800/515288.
[5] Miró L, Gasia J, Cabeza LF. Thermal energy storage (TES) for industrial waste heat (IWH) recovery: A review. Appl Energy 2016;179:284–301. https://doi.org/10.1016/j.apenergy.2016.06.147.
[6] Lund H, Østergaard PA, Connolly D, Ridjan I, Mathiesen BV, Hvelplund F, et al. Energy Storage and Smart Energy Systems. Int J Sustain Energy Planning Manage 2016;11:3–14. https://doi.org/10.5278/ijsepm.2016.11.2.
[7] Vecchi A, Sciacovelli A. Long-duration thermo-mechanical energy storage – Present and future techno-economic competitiveness. Appl Energy 2023;334. https://doi.org/10.1016/j.apenergy.2022.120628.
[8] A. V. Olympios, J. D. McTigue, P. Farres-Antunez, A. Tafone, A. Romagnoli, Y. Li, Y. Ding, W.-D. Steinmann, L. Wang, H. Chen, and C. N. Markides, "Progress and prospects of thermo-mechanical energy storage—a critical review", *Progress in Energy,* vol. 3, no. 2, 2021, doi: 10.1088/2516-1083/abdbba.
[9] Vecchi A, Knobloch K, Liang T, Kildahl H, Sciacovelli A, Engelbrecht K, et al. Carnot Battery development: A review on system performance, applications and commercial state-of-the-art. J Storage Mater 2022;55. https://doi.org/10.1016/j.est.2022.105782.
[10] O. Dumont, G. F. Frate, A. Pillai, S. Lecompte, M. De paepe, and V. Lemort, "Carnot battery technology: A state-of-the-art review", *Journal of Energy Storage,* vol. 32, 2020, doi: 10.1016/j.est.2020.101756.
[11] Tian W, Xi H. Comparative analysis and optimization of pumped thermal energy storage systems based on different power cycles. Energ Conver Manage 2022;259. https://doi.org/10.1016/j.enconman.2022.115581.
[12] Sun R, Zhao Y, Liu M, Yan J. Thermodynamic design and optimization of pumped thermal electricity storage systems using supercritical carbon dioxide as the working fluid. Energ Conver Manage 2022;271. https://doi.org/10.1016/j.enconman.2022.116322.
[13] S. Staub, P. Bazan, K. Braimakis, D. Müller, C. Regensburger, D. Scharrer, B. Schmitt, D. Steger, R. German, S. Karellas, M. Pruckner, E. Schlücker, S. Will, and J. Karl, "Reversible Heat Pump–Organic Rankine Cycle Systems for the Storage of Renewable Electricity", *Energies,* vol. 11, no. 6, 2018, doi: 10.3390/en11061352.
[14] Steinmann W-D. Thermo-mechanical concepts for bulk energy storage. Renew Sustain Energy Rev 2017;75:205–19. https://doi.org/10.1016/j.rser.2016.10.065.
[15] Zhao Y, Song J, Zhao C, Zhao Y, Markides CN. Thermodynamic investigation of latent-heat stores for pumped-thermal energy storage. J Storage Mater 2022;55. https://doi.org/10.1016/j.est.2022.105802.
[16] Hu S, Yang Z, Li J, Duan Y. Thermo-economic analysis of the pumped thermal energy storage with thermal integration in different application scenarios. Energ Conver Manage 2021;236. https://doi.org/10.1016/j.enconman.2021.114072.
[17] Dumont O, Lemort V. Mapping of performance of pumped thermal energy storage (Carnot battery) using waste heat recovery. Energy 2020;211. https://doi.org/10.1016/j.energy.2020.118963.
[18] Frate GF, Ferrari L, Desideri U. Multi-Criteria Economic Analysis of a Pumped Thermal Electricity Storage (PTES) With Thermal Integration. Front Energy Res 2020;8. https://doi.org/10.3389/fenrg.2020.00053.
[19] Zhang M, Shi L, Zhang Y, He J, Sun X, Hu P, et al. Configuration mapping of thermally integrated pumped thermal energy storage system. Energ Conver Manage 2023;294. https://doi.org/10.1016/j.enconman.2023.117561.
[20] Benato A, Stoppato A. Pumped Thermal Electricity Storage: A technology overview. Thermal Science and Engineering Progress 2018;6:301–15. https://doi.org/10.1016/j.tsep.2018.01.017.
[21] G. F. Frate, L. Ferrari, and U. Desideri, "Rankine Carnot Batteries with the Integration of Thermal Energy Sources: A Review", *Energies,* vol. 13, no. 18, 2020, doi: 10.3390/en13184766.
[22] Steinmann WD. The CHEST (Compressed Heat Energy STorage) concept for facility scale thermo mechanical energy storage. Energy 2014;69:543–52. https://doi.org/10.1016/j.energy.2014.03.049.
[23] A. Tafone, R. Pili, M. Pihl Andersen, and A. Romagnoli, "Dynamic modelling of a compressed heat energy storage (CHEST) system integrated with a cascaded phase change materials thermal energy storage", *Applied Thermal Engineering,* vol. 226, 2023, doi: 10.1016/j.applthermaleng.2023.120256.
[24] Jockenhöfer H, Steinmann W-D, Bauer D. Detailed numerical investigation of a pumped thermal energy storage with low temperature heat integration. Energy 2018;145:665–76. https://doi.org/10.1016/j.energy.2017.12.087.
[25] Hassan AH, O'Donoghue L, Sánchez-Canales V, Corberán JM, Payá J, Jockenhöfer H. Thermodynamic analysis of high-temperature pumped thermal energy storage systems: Refrigerant selection, performance and limitations. Energy Rep 2020;6:147–59. https://doi.org/10.1016/j.egyr.2020.05.010.
[26] Frate GF, Antonelli M, Desideri U. A novel Pumped Thermal Electricity Storage (PTES) system with thermal integration. Appl Therm Eng 2017;121:1051–8. https://doi.org/10.1016/j.applthermaleng.2017.04.127.
[27] Lund R. Energy System Benefits of Combined Electricity and Thermal Storage Integrated with District Heating. Int J Sustain Energy Planning Manage 2021;31:23–38. https://doi.org/10.5278/ijsepm.6273.
[28] V. Sánchez-Canales, J. Payá, J. M. Corberán, and A. H. Hassan, "Dynamic Modelling and Techno-Economic Assessment of a Compressed Heat Energy Storage System: Application in a 26-MW Wind Farm in Spain", *Energies,* vol. 13, no. 18, 2020, doi: 10.3390/en13184739.
[29] V. Novotny, V. Basta, P. Smola, and J. Spale, "Review of Carnot Battery Technology Commercial Development", *Energies,* vol. 15, no. 2, 2022, doi: 10.3390/en15020647.
[30] Steinmann W-D, Bauer D, Jockenhöfer H, Johnson M. Pumped thermal energy storage (PTES) as smart sector-coupling technology for heat and electricity. Energy 2019;183:185–90. https://doi.org/10.1016/j.energy.2019.06.058.
[31] Arpagaus C, Bless F, Uhlmann M, Schiffmann J, Bertsch SS. High temperature heat pumps: Market overview, state of the art, research status, refrigerants, and application potentials. Energy 2018;152:985–1010. https://doi.org/10.1016/j.energy.2018.03.166.
[32] Gueani M, Zamali H, Jimal M. Diagramme de phases LiNO3-KNO3. Solid state chemistry and crystal chemistry 1998;2:787–9.
[33] Tamme R, Bauer T, Buschle J, Laing D, Müller-Steinhagen H, Steinmann W-D. Latent heat storage above 120°C for applications in the industrial process heat sector and solar power generation. Int J Energy Res 2008;32(3):264–71. https://doi.org/10.1002/er.1346.
[34] Roget F, Favotto C, Rogez J. Study of the KNO3–LiNO3 and KNO3–NaNO3–LiNO3 eutectics as phase change materials for thermal storage in a low-temperature solar power plant. Sol Energy 2013;95:155–69. https://doi.org/10.1016/j.solener.2013.06.008.
[35] Cotter DF, Shah NN, Huang MJ, Hewitt NJ. "Refrigerant lubricant interaction in high-temperature heat pump and organic Rankine cycle systems," presented at the IIR International Rankine 2020 Conference -Heating, Cooling and Power Generation, Glasgow. UK July 2020;26–29. https://doi.org/10.18462/iir.rankine.2020.1198.
[36] *Reference Fluid Thermodynamik and Transport Properties (REFPROP)*. (2018). Standard Reference Database 23, DLL version number 10.0. National Institute of Standards and Technology (NIST), E. W. Lemmon, I. H. Bell, M. L. Huber, and M. O. McLinden. Boulder, Colorado.
[37] Hassan AH, Corberán JM, Ramirez M, Trebilcock Kelly FT, Payá J. A high-temperature heat pump for compressed heat energy storage applications: Design, modeling, and performance. Energy Rep 2022;8:10833–48. https://doi.org/10.1016/j.egyr.2022.08.201.
[38] Ramirez M, Trebilcock Kelly FT, Corrales Ciganda JL, Payá J, Hassan AH. Experimental and numerical investigation of a novel high-temperature heat pump for sensible and latent heat delivery. Appl Therm Eng 2024. https://doi.org/10.1016/j.applthermaleng.2024.122961.
[39] P. Arora, G. Seshadri, and A. K. Tyagi, "Fourth-Generation Refrigerant:HFO 1234yf", *Current Science,* vol. 115, no. 8, 2018, doi: 10.18520/cs/v115/i8/1497-1503.
[40] Johnson M, Vogel J, Hempel M, Hachmann B, Dengel A. Design of high temperature thermal energy storage for high power levels. Sustain Cities Soc 2017;35:758–63. https://doi.org/10.1016/j.scs.2017.09.007.

[41] Li Q, Li C, Du Z, Jiang F, Ding Y. A review of performance investigation and enhancement of shell and tube thermal energy storage device containing molten salt based phase change materials for medium and high temperature applications. Appl Energy 2019;255. https://doi.org/10.1016/j.apenergy.2019.113806.
[42] Johnson M, Hübner S, Braun M, Martin C, Fiß M, Hachmann B, et al. Assembly and attachment methods for extended aluminum fins onto steel tubes for high temperature latent heat storage units. Appl Therm Eng 2018;144:96–105. https://doi.org/10.1016/j.applthermaleng.2018.08.035.
[43] Couvreur K, Tassenoy R, van Heule X, De Paepe M, Lecompte S. Experimental and numerical analysis of variable volume ratio as additional optimization parameter in organic Rankine cycle expanders. Appl Therm Eng 2022;216. https://doi.org/10.1016/j.applthermaleng.2022.119007.
[44] Glushenkov M, Kronberg A. Experimental study of an isobaric expansion engine-pump – Proof of concept. Appl Therm Eng 2022;212. https://doi.org/10.1016/j.applthermaleng.2022.118521.